https://doi.org/10.1016/j.jclepro.2021.127996

Transforming natural silk nonwovens into robust bioadhesives for in vivo tissue amendment

Chunhong Yang[a, c], Songmin Shang [b], Dahua Shou [b], Luoxiao Ran [a, c], Guangqian Lan [a, c] and Enling Hu [a, b, c, *]

[a] *State Key Laboratory of Silkworm Genome Biology, College of Sericulture, Textile and Biomass Sciences, Southwest University, Chongqing 400715, China*

[b] *Institute of Textiles and Clothing, The Hong Kong Polytechnic University, Kowloon, Hong Kong*

[c] *Chongqing Engineering Research Center of Biomaterial Fiber and Modern Textile, Chongqing 400715, China*

***Corresponding author:**

Email: enling.allen.hu@connect.polyu.hk (Enling Hu)

Address:

Dr Enling Hu

Institute of Textiles and Clothing

Room QT715, Q Core, 7/F

The Hong Kong Polytechnic University

Hunghom, Kowloon

Hong Kong

ABSTRACT

Textile manufacturing of silk generates unwindable raw silk fibers, which are treated as silk wastes for downcycling applications, thus unexpectedly demoting the luxury status of silk. As a primary trial seeking to reshape the destiny of silk wastes, the present study is focused on transforming natural silk nonwovens, as a typical model of artificial silk nonwovens, into bioadhesives for tissue repair. Herein, a technique is demonstrated for the preparation of a transparent and stretchable adhesive from a silkworm cocoon sheet (SCS), a typical natural silk nonwoven. This technique differs from the traditional method of completely dissolving silk fibers to obtain silk fibroin. Specifically, the technique entailed pretreatment of the SCS with a $CaCl_2$-ethanol-H_2O ternary solution to obtain a modified cocoon sheet (MCS), followed by surface modification with a $CaCl_2$-formic acid (Ca-FA) solution to obtain MCS@Ca with controllable adhesion, which was achieved by adjusting the Ca^{2+} content in Ca-FA. The highly stretchable MCS@Ca firmly adhered to various substrates for loads as high as 54 kPa, and its performance in repairing an injured liver *in vivo* was superior to that of a commercial product, Sorbalgon®. Additionally, MCS@Ca effectively sealed a freshly punctured porcine heart and stomach *ex vivo*, thereby demonstrating its potential as a sealant. To our knowledge, this is the first study on upcycling disqualified silk fibers using a convenient top-down approach to prepare robust bioadhesives for tissue repair, wherein MCS@Ca may serve to bridge the gap between advanced biomaterials and disqualified silk wastes.

Keywords: Silk wastes, upcycling, silk fibroin, bioadhesives, tissue repair, textile nonwovens

1. Introduction

Silk is a natural protein fiber that has been used for luxurious textiles for thousands of years. A network of trade routes, the Silk Road, was established as early as the Han dynasty of China (207 BCE–220 CE) to connect ancient China, South Asia, Central Asia, East Africa, and Southern Europe for the trading of luxurious silk textiles and other rare goods (Huadong, 2018), which was lucrative because throughout human civilization, luxurious silk textiles have been inextricably linked to wealth owing to their high market value based on their superior properties, such as smoothness, luster, and comfort (Wei et al., 2018). In textile manufacturing, some unwindable short-length silk fibers are generated before/during/after silk yarn spinning. Because of their limited length or strength, these abundant silk fibers are generally treated as waste (known as silk wastes or waste silk) and down-recycled by blending with low-price textile fibers for conventional textile manufacturing, thus devaluing silk textiles. Although the demand for silk textiles has gradually reduced in the modern era due to the emergence of silk-like synthetic fibers, the development of silk materials in advanced applications has rapidly increased.

Specifically, silk has been used in biomedical applications because of its varied sources, good biocompatibility (Kim et al., 2020), and tunable mechanical properties (Huang et al., 2020). The excellent air permeability of silk membranes under wet conditions, which resembles that of the human skin, is an advantage for its potential application in bioengineering (Johnston et al., 2018). Natural silk fiber typically consists of two parts: the silk fibroin (SF) core and the silk sericin (SS) peel (Wang et al., 2019b). Since it is a renewable protein-based material, SF has been extensively used as a key component in various biomaterials, such as wound dressings, surgical threads, and implanted

scaffolds. Even though some silk biomaterials are used in the form of fibers or textiles (Zhou et al., 2020), the majority of applications use regenerated SF materials, which applies a bottom-up strategy to remodel totally dissolved silk.

Immediate closure of a wound after surgery or trauma is essential to promote healing and prevent infection (Annabi et al., 2017). Sutures are commonly used to close wounds because of their high tensile strength and associated low rate of dehiscence (Ghobril and Grinstaff, 2015). Nevertheless, sutures are imperfect as they have certain inherent disadvantages: (1) the application of sutures causes pain to patients and requires technical skills, which vary widely from one surgeon to another, influencing the success of the procedure (Chen et al., 2017); (2) suture stitching is a time-consuming procedure (Cui et al., 2020); and (3) the use of sutures carries risks of inflammation, nerve damage, infection, and formation of scar tissue (He et al., 2020), resulting from tissue penetration (Costa et al., 2019). Bio-staple stitching, which has been introduced as a convenient and fast alternative to conventional sutures, can be readily applied without the need for sophisticated practical skills and with a lower associated risk of infection (Chen et al., 2020). However, this approach also requires anesthetics and may generate an imprecise wound approximation (Han et al., 2017). Hence, there remains a need to develop safe, simple, and non-invasive alternative wound closure materials. To this end, the following considerations are necessary: 1) the developed material must be able to securely adhere to the wound site, even under moist conditions, while maintaining mechanical strength (Xu et al., 2018); 2) the adhesive must provide complete coverage to seal the wound and prevent gas or fluid leakage (Guo et al., 2017); 3) the application of the adhesive must be simple (Ryu et al., 2019); and 4) the adhesive must possess excellent biocompatibility and biodegradability.

Many research groups continue to work toward the development of new and effective bioadhesives. For instance, a robust adhesive hydrogel was recently developed for wet tissues, which was capable of withstanding high blood pressures (290 mmHg) to stop bleeding from pig carotid arteries and hearts (Hong et al., 2019). Additionally, Qiao et al. reported a sponge adhesive with strong wet tissue adhesion properties capable of rapidly sealing wounds and achieving remarkable hemorrhage control in one minute (Liu et al., 2019). In addition to these attempts, SF can also be used to produce adhesives. It is interesting to note that SF can coordinate with other molecules to alter its adhesive properties, such as hydrophilic polyethylene glycol (Burke et al., 2016), tannic acid (Bai et al., 2019b), and calcium ions (Ca^{2+}) (Zhang et al., 2015a). For example, Ca^{2+}-modified silk protein demonstrated high adhesion performance on epidermis (Seo et al., 2018). Inspired by this attempt, SF adhesives was investigated for wound closures as a similar SF hydrogel adhesive was shown to seal bleeding wounds for hemostasis (Bai et al., 2019a). However, these preparations involve complex bottom-up processes in which remodeling of the totally dissolved SF is inevitable, and the complex total dissolution process may be harmful to the environment (Ming et al., 2018), which are not in line with the concept of green or ecology (Zhang, 2020; Zhang et al., 2021). In addition, the complicated preparation processes and massive energy consumption discourage high yield (Zhang et al., 2015b) and large-scale applications (Zhang, 2021). More importantly, films or membranes regenerated from totally dissolved SF solutions may lack robust mechanical properties, thus limiting their applications, especially in situations involving twisting, stretching, or dynamic bursting by either liquid or gas. Hence, the research community has gradually moved away from the typical bottom-up strategy toward a top-down design approach, which could provide reinforced SF adhesives for tissue repair and is more effective and sustainable (Sun et al., 2020).

Therefore, in this study, a highly robust Janus SF adhesive with single-sided wet adhesion was prepared using silkworm cocoon sheets (SCS) via a top-down approach. SCS was adopted as a typical raw material of natural silk nonwovens because it is remarkably similar to artificial silk nonwovens made from silk wastes. Here, we prepared a Ca^{2+}-modified cocoon sheet (MCS@Ca) based on two criteria: (i) facile top-down approach and (ii) robust adhesion to wet tissue. The first criterion was achieved *via* pretreatment with a $CaCl_2$-ethanol-H_2O ternary solution (TS), which retained the integrity of the original material, thus laying the foundation for controllable adhesion. The second criterion can be met by surface modification of the adhesive with Ca-formic acid (FA). Considering that the different mass fractions of FA and $CaCl_2$ in Ca-FA led to different adhesive strengths, adjusting the $CaCl_2$:FA ratio in Ca-FA may provide controllable adhesion of MCS@Ca. A schematic of the preparation process is illustrated in Figure 1. Step 1 focuses on preparing the modified cocoon sheets (MCS) by pretreatment of SCS with the TS, which is followed by Step 2, which involves the surface modification of Ca-FA over a single MCS surface to create strongly adhesive MCS@Ca for wet tissues. To examine the practical performance of the SF adhesive, *in vivo* rabbit liver healing and biodegradation tests were carried out.

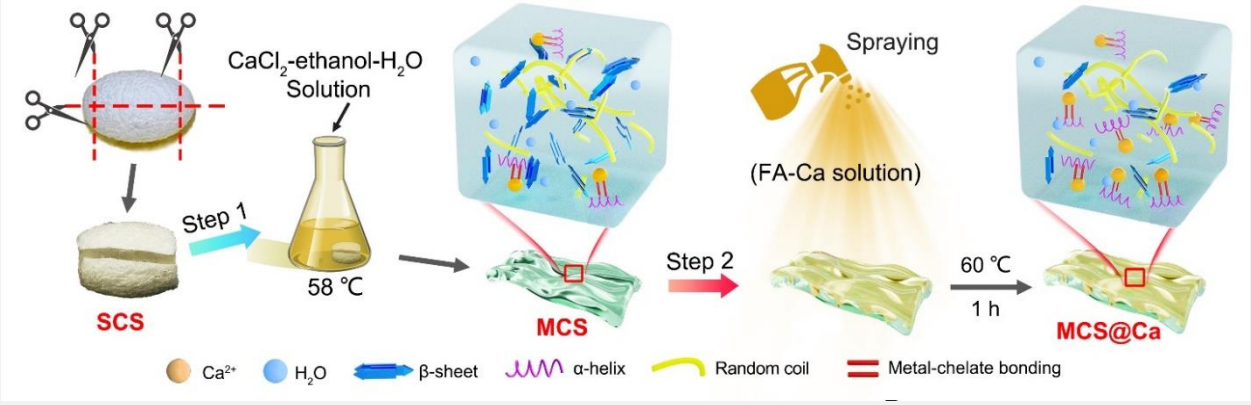

Figure 1. Schematic of the transformation of natural silk nonwovens, silkworm cocoon sheets (SCS), to modified cocoon sheets (MCS) and then bioadhesives (MCS@Ca).

This was the first attempt at using natural silk nonwovens via a facile top-down method to prepare robust bioadhesives for the repair of damaged tissue. The top-down approach not only has the advantage of simplicity but also maintains the integrity of the original material. More importantly, the present study may offer a new perspective to re-shape the destiny of silk wastes. The situation where disqualified silk fibers (unwindable silk wastes) are downcycled into low-value textiles may change since silk wastes can be easily processed into artificial silk nonwovens for the production of advanced silk biomaterials *via* a facile top-down approach. As artificial silk nonwovens require only short and weak fibers, the present study may provide a platform for the upcycling of silk wastes at the industrial scale, thus improving the sustainability of both the textile industry and biomaterial manufacturing. Moreover, the concept of "wastes-to-resources" presented in this study may promote the establishment of a totally new supply chain for the manufacture of biomaterials using silk wastes.

2. Materials and Methods

2.1 Reagents and Materials

Unless otherwise indicated, all the chemicals were commercially available, of analytical reagent grade, and used without further purification. *Bombyx mori* cocoons were provided by High Fashion International Limited (New Territories, Hong Kong). New Zealand rabbits were provided by the Animal Laboratory Center of the Third Military Medical University (Chongqing, China). All the animal experiments were approved by Southwest University Animal Ethics Committee and were performed in accordance with the protocols approved by the National Teaching Center of Animal Science and Experiment of Southwest University, China (accreditation number of the investigator:

CQLA-2019-0281).

2.2 Preparation of MCS@Ca

The two ends of the *Bombyx mori* cocoons were cut to remove the silkworm chrysalis, from which SCS were obtained. Subsequently, TS (molar ratio of $CaCl_2$:ethanol:H_2O = 1:2:8) was used to treat the SCS (58 °C, 30 min). After removing the TS with deionized water, the as-prepared modified cocoon sheet (MCS) was obtained. Next, the MCS was sprayed with a Ca^{2+}-containing FA solution (Ca-FA) with different mass fractions (weight ratio of $CaCl_2$:formic acid = 10:90, 20:80, 30:70) and kept at 65 °C for 1 h. The residual FA was then removed *via* natural evaporation at 25 °C for 7 d; a series of MCS@Ca materials was subsequently obtained. According to the above-mentioned mass fractions of Ca-FA, the MCS@Ca materials were denoted as MCS@Ca10, MCS@Ca20, and MCS@Ca30, respectively.

2.3 Characterization of materials

Raman spectra of SCS, MCS, and MCS@Ca were measured using a Raman spectrometer (Renishaw, Invia, England). Changes in the chemical groups of the samples were evaluated by Fourier transform infrared spectroscopy (FTIR) (ALPHA, Karlsruhe, Germany). Frequency sweeps were scanned using an advanced rheometer (MCR102, Anton Par, Austria). Ultraviolet (UV) absorption spectra were obtained using a UV-vis diffuse reflectance spectrometer (UV2600, SIMADZU, Japan). Field emission scanning electron microscopy (SEM; SEM450, Thermo Fisher, America) images were used to determine the morphology. Optical and fluorescence microscope images of MCS@Ca20 adhered to porcine skin after 1 min and 1 h were collected using a digital microscope (CKX53, Olympus, Japan). The transmittances of MCS and MCS@Ca20 were determined using a microplate reader

(Synergy LX, BioTek, USA). To assess the air-sealing capacity of MCS@Ca20, a standard balloon was used.

2.4 Viscoelasticity tests

The viscoelastic properties of the samples were evaluated using a rheometer (MCR102, Anton Par, Graz, Austria). The samples (1.5 × 1.5 cm) were loaded on the bottom metal plate and sandwiched by the top plate. The storage modulus (G′), loss modulus (G″), and viscosity were measured in the angular frequency (ω) range of 0.1 to 100 rad/s with a fixed strain of 1%.

2.5 Mechanical tests

Stress–strain tests of MCS@Ca were performed on an electronic universal tension machine (AGS-X, Shimadzu, Japan). All the samples were 15-mm wide, 2-mm thick, and 30-mm long, with a testing gauge length of 20 mm. At least five measurements were performed per sample. The Young's modulus was defined as the initial elastic deformation area of the stress–strain curve.

2.6 Adhesion tests

Porcine skin tissue was used for its robust mechanical property and close resemblance to human skin. Before the tests, all the samples were completely adhered to the porcine skin tissue under a force of 20 N for 15 s, and all the tests were performed using an electronic universal tension machine (AGS-X, Shimadzu, Japan) at a constant tensile speed (10 mm min^{-1}). For the lap shear test, the samples were cut into a rectangle (10 mm in width and 20 mm in length), while for the recuperative and repeatable cyclic adhesion tests, circular samples with a 2-cm radius were used. In the recuperative test, for the first loading test, MCS@Ca was placed over porcine skin, which had been fixed over

holder A, and was subsequently pressed by another piece of porcine skin that was fixed to the bottom of holder B with a force of 20 N for 15 s. After 2 min, the two porcine skins were separated following removal of the applied force, and MCS@Ca was kept at 25 °C for 1 h to allow it to recover to the original state. Subsequently, the second loading test was carried out in the same way as the first. In the repeatable cyclic adhesion test (repeated continuous adhere-detach test), detachment was performed 5 s after adhesion in each dependent testing cycle and 5-s intervals were used between two joint cycles. The tensile strength and shear strength (pressure) were calculated by dividing the maximum force by the adhesion area.

2.7 Cytotoxicity assay

Cytocompatibility was evaluated using a live/dead cell staining assay for fibroblasts. Briefly, mouse skin fibroblasts (L929 cells) were mixed into a single cell suspension containing 3% gentamicin and 10% fetal calf serum. The cell suspension was then transferred to a 96-well plate at 37 °C. When the cells were attached, the cell suspension was blended with the samples at 37 °C for 24 h to obtain a precursor solution with a final cell density of 2.5×10^4 mL^{-1}. Cell viability was then determined via microscopic imaging. For the MTT assay, when the mixtures were seeded into a 48-well plate (200 mL $well^{-1}$), the cells were cultured at 37 °C for 24 and/or 48 h after adding the MTT solution (10 μL). Dimethyl sulfoxide (DMSO) was subsequently added after the medium was removed. Finally, the absorbance was measured at 450 nm.

2.8 In vivo rabbit liver healing studies

Six female rabbits were used for the liver healing study. A 3-cm incision was made in the rib cage of each rabbit, after which an 8-mm cut was produced in the rabbit liver, and MCS@Ca20 was applied

to the wound. Finally, the MCS@Ca20-applied rabbit liver was inserted back into the rabbit, and the wound in the rib cage was sutured. The rabbits were euthanized on days 14, 28, and 42, and the MCS@Ca20-applied liver was collected and soaked in a formaldehyde solution (10%). To visualize wound collagen fiber sections, hematoxylin and eosin (H&E) staining was used. Histological sections were observed using a digital microscope (CKX53, Olympus, Japan).

2.9 In vivo degradation in back muscles

Eight female rabbits were used in the back muscle biodegradation experiment. A 2-cm cut per animal was created in the muscles on either side of the subcutaneous pockets of each rabbit. Sorbalgon dressing (Sorbalgon®) and MCS@Ca20 were then implanted into the dorsal subcutaneous pockets under sterile conditions (1 cm × 1 cm). After suturing the wound, antibiotics (gentamycin sulfate, 2.5 mg) were administered to each rabbit. The rabbits were euthanized on days 14, 28, 42, and 56, and muscle samples at and around the implant site were collected for histological analysis using the same instrument mentioned above.

2.10 Ex vivo tests

A hole (diameter, 8 mm) was first made in the porcine stomach. Then, MCS@Ca20 was placed over the damaged area to cover the puncture hole by applying slight pressure for 5 s. Thereafter, the porcine stomach was continuously injected with water to monitor liquid leakage. For the heart test, the same piercing treatment was applied to produce a hole over the porcine heart. Subsequently, the punctured heart was sealed with MCS@Ca20, of which the front side was attached with a pressure sensor. Thereafter, the left atrium and ventricle were filled with red ink through the pulmonary veins. When all the inlet and outlet vessels were blocked, which prevented leaking of red ink, a periodic pressure

was applied to the heart to mimic the heartbeat. During the continuous beating, pressure at the punctured site of the heart was recorded. A sensor was attached to the surface of MCS@Ca20 to sense changes in pressure for 20 cycles.

3. Results and Discussion

3.1 Characterization of MCS@Ca

SCS were adopted as the typical natural silk nonwovens. They were first pre-treated with the TS to remove SS and then superficially modified with Ca^{2+}-FA on one side to achieve single-sided tractable adhesion. As illustrated in Figure 1**,** by exploiting the interaction between Ca^{2+} and SF, the prepared functional MCS@Ca can be utilized as adhesives or sealants in tissue repair. The effect of TA and Ca-FA on MCS@Ca was first examined using SEM. Freeze-dried SCS possessed a structure of entangled fibers with rich macro-chambers (Figure 2A) and became porous when soaked in TA (Figure 2B). However, following the Ca-FA treatment, the porous structure disappeared, and the surface of MCS@Ca became smooth, indicating that dissolution by FA affected the surface morphology of MCS@Ca. Although the porous structure of MCS@Ca was destroyed upon exposure to Ca-FA, more than 70% transparency remained (Figure 2C).

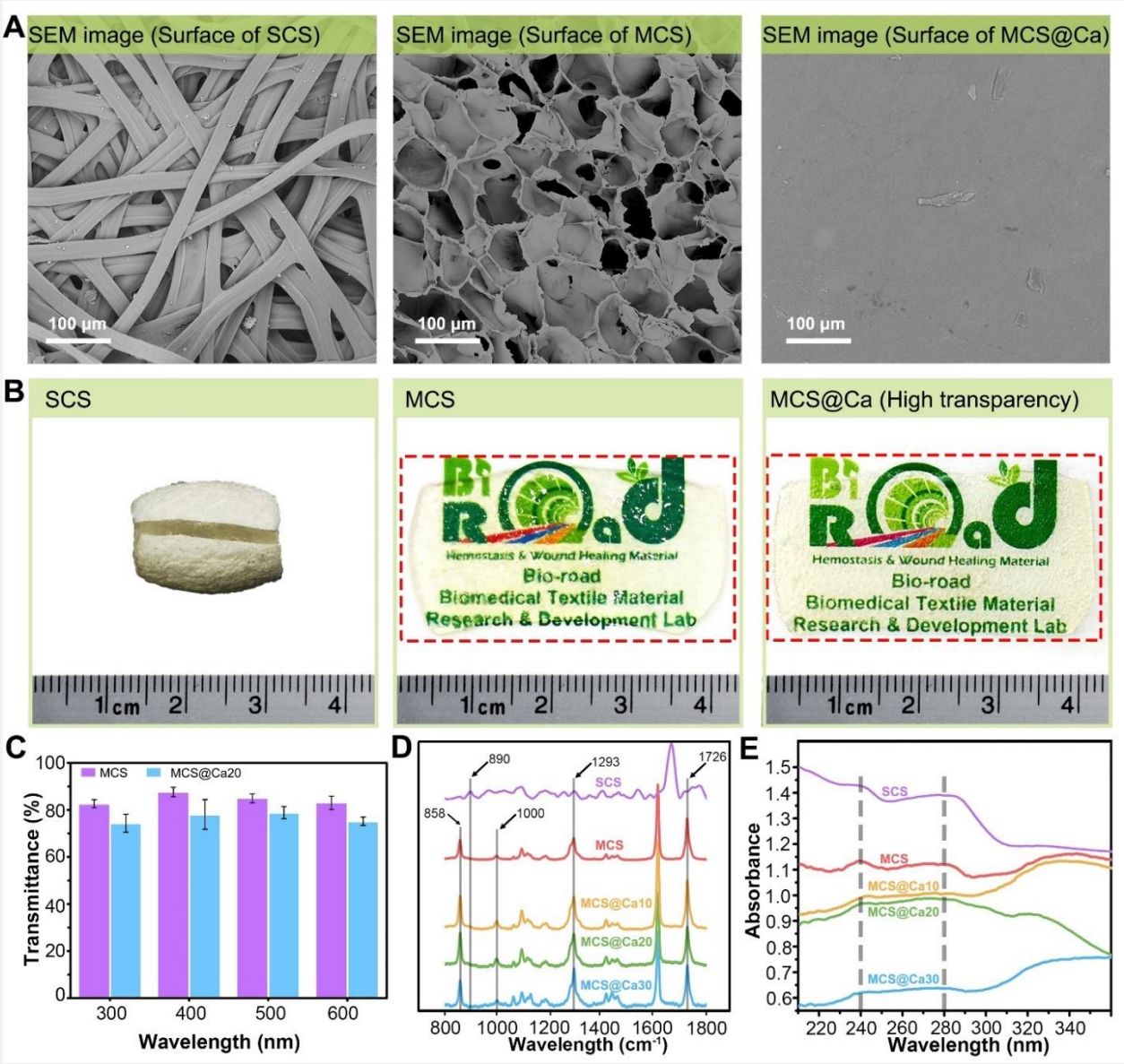

Figure 2. A) SEM images. B) Digital images. C) Optical transparency measured at various wavelengths. D) Raman spectra. E) Ultraviolet absorption spectra.

The effect of Ca-FA on the chemical structure of SF was examined using Raman spectroscopy (Figure 2D). The 1620–1720 cm^{-1} peak was attributed to amide I, while the 1250–1360 cm^{-1} peak was assigned to amide III (Cheng et al., 2019). As shown in Figure 2D, MCS, MCS@Ca10, MCS@Ca20, and MCS@Ca30 all had distinctive absorption at 858 cm^{-1}, corresponding to the tyrosine peak (Taddei et al., 2017). Previous studies have confirmed that tyrosine in SF plays an important role in

273 Ca^{2+} chelating (Drnovšek et al., 2016); Ca^{2+} may chelate with SF through the amine group on the
274 tyrosine residues in MCS and the environment surrounding tyrosine becomes more hydrophobic,
275 which then serves to enhance intermolecular hydrogen bonding (Deng et al., 2019). Furthermore,
276 benzene rings (1000 cm^{-1}), which can cooperate with amino acids for adhesion (Wei et al., 2016),
277 were also present in SF after the Ca-FA treatment, as shown in Figure 2D. Thus, tyrosine in SF, which
278 was treated with different mass fractions of FA and $CaCl_2$, is critical for regulating the underlying
279 interactions that contribute to adhesion.
280
281 The role of Ca^{2+} in the treatment of SCS was also examined by UV spectrophotometry. In Figure 2E,
282 the two prominent peaks at approximately 240 nm and 280 nm represent the carboxyl and tyrosine
283 groups of SF, respectively (Qiu et al., 2019; Sun and Marelli, 2020). The change in the intensity of
284 the 240-nm peak was mainly due to the polarization change of the carboxyl group caused by the
285 formation of a Ca^{2+} metal–chelate bond with the carboxyl groups of silk fibroin; in addition, the water
286 molecules captured by Ca^{2+} likely hindered the formation of hydrogen bonds between the polar
287 groups in SF and the tyrosine groups (Seo et al., 2018), resulting in the blue-shift of the tyrosine peak
288 (at approximately 286 nm for MCS) to 280 nm. The changes in the peak positions and intensities
289 indicated that Ca^{2+} interacted with the amino acids in SF.
290
291 FTIR was used to further examine the effect of Ca^{2+} on SCS. The FTIR spectrum of SCS contained
292 peaks at 1508 and 1618 cm^{-1} due to N–H bending and C=O stretching, respectively (Jin et al., 2005).
293 Compared with SCS, the FTIR peaks of MCS@Ca shifted to 1587 cm^{-1} (N–H) and 1637 cm^{-1} (C=O),
294 which could be ascribed to the chelating reactions between Ca^{2+} and the carboxyl (-COOH), amino
295 ($-NH_2$), and imino (-NH) groups of the peptides in SF (Lin et al., 2015). Furthermore, the interaction

between Ca^{2+} and SF also affected the secondary structure of SF. Figure 3B-F shows deconvoluted amide I region (1580~1720 cm^{-1}) of the different samples, and Figure 3G summarizes the random coil, β-sheet, and β-turn contents. After the TS treatment, the β-sheet content in MCS increased from that of SCS (Figure 3G). In addition, after the FA-Ca treatment, the random coil content also increased. The change in secondary structure indicated that treatment with FA-Ca could lead to a high random coil content in SF.

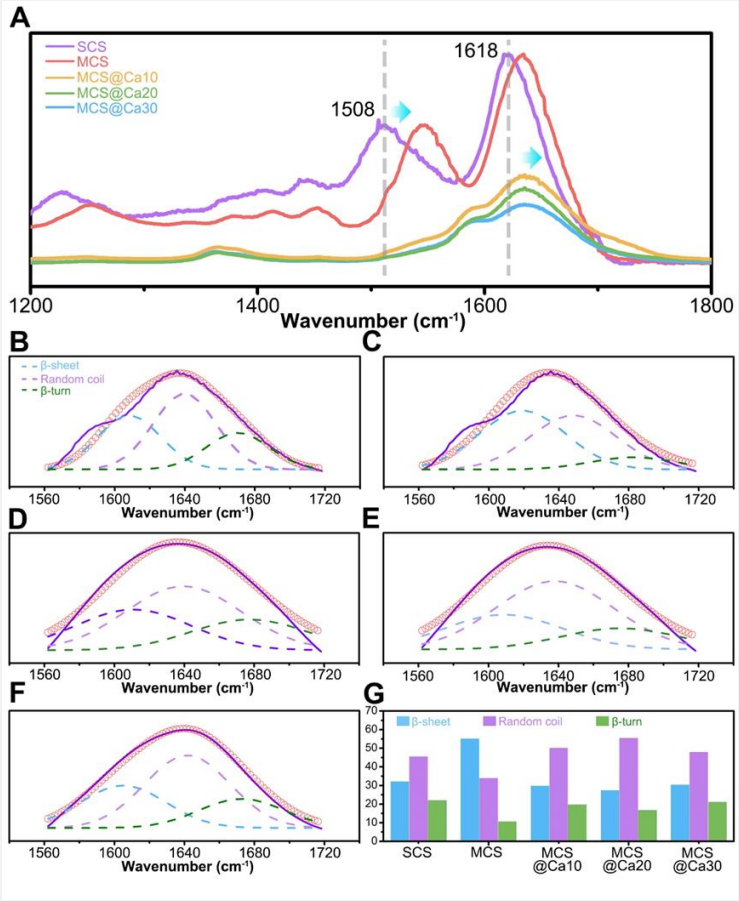

Figure 3. A) FTIR spectra. Deconvolution of the amide I region (1580~1720 cm^{-1}): B) SCS, C) MCS, D) MCS@Ca10, E) MCS@Ca20 and F) MCS@Ca30. G) Random coil, β-sheet, and β-turn contents from the deconvolution of the amide I peak.

3.2 Adhesion assessment ex vivo

As mentioned above, the chelation of Ca^{2+} with the amino acid in SF, such as tyrosine, causes the polypeptide chains to undergo a conformational transformation, thus generating adhesive properties. Phenolic hydroxyl and amino acids act as hydrogen donors, promoting biological adhesion through van der Waals forces and hydrogen bonding (Brennan et al., 2017). Furthermore, the benzene rings close to the surface of MCS@Ca can bind to hydrophobic substrates through cationic or π–π interactions upon contact. Subsequently, van der Waals forces, hydrogen bonding, and/or π–π interactions between SF and the tissue surface can further improve the strength and adhesive stability of MCS@Ca (Johnston et al., 2018). To evaluate the adhesion of MCS@Ca, the lap shear adhesive strength was quantified using the self-established model, as shown in Figure 4A. Although all the MCS@Ca materials exhibited adhesive properties because of the water-capturing and metal-chelating properties of Ca^{2+}, their adhesion performance on porcine skin differed. In particular, MCS@Ca20 exhibited superior adhesive performance (approximately 54 kPa; Figure 4B). The different adhesion performances of the materials could be attributed to the change in Ca^{2+} content. Both an excessive and an insufficient Ca^{2+} content decreases the adhesion performance of MCS@Ca, mainly due to the following reasons. When the Ca^{2+} content in MCS@Ca is low, the amino acid groups in SF prefer to bond with Ca^{2+} instead of the water molecules, allowing Ca^{2+} to chelate with the random coil chains in SF to provide suitable cohesion and energy dissipation, which is related to adhesion (Kim et al., 2018). However, when a large amount of Ca^{2+} is present, Ca^{2+} induced over-capture of water molecules may occur, which impedes Ca^{2+} from coordinating with the amino acid groups and resulting in a moderate decrease in adhesive strength. Furthermore, studies have shown that Ca^{2+} hinders the formation of β-sheets (Ling et al., 2016) and increase the random coil content (Seo et al., 2018). Therefore, MCS@Ca20 contained the highest random coil content and the lowest β-sheet content (Figure 3G), leading to the best adhesion performance (Figure 4B). All the experimental

results showed that MCS@Ca20 possessed the optimum Ca^{2+} content, which led to superior adhesion performance. Compared with similar materials used for tissue adhesion, the adhesive strength of MCS@Ca20 (54 KPa) was better than that of previously reported adhesives, including the dynamic hydrophobic hydrogel (approximately 31 KPa) (Han et al., 2020), the dual-adhesive and bioactive hydrogel (approximately 51 KPa) (Gao et al., 2019), and the bioadhesives derived from the skin secretion of *Andrias davidianus* (approximately 26 KPa) (Deng et al., 2019). In addition to bio-applications, MCS@Ca20 was also competitive against certain reported materials for wet adhesion (Li et al., 2017).

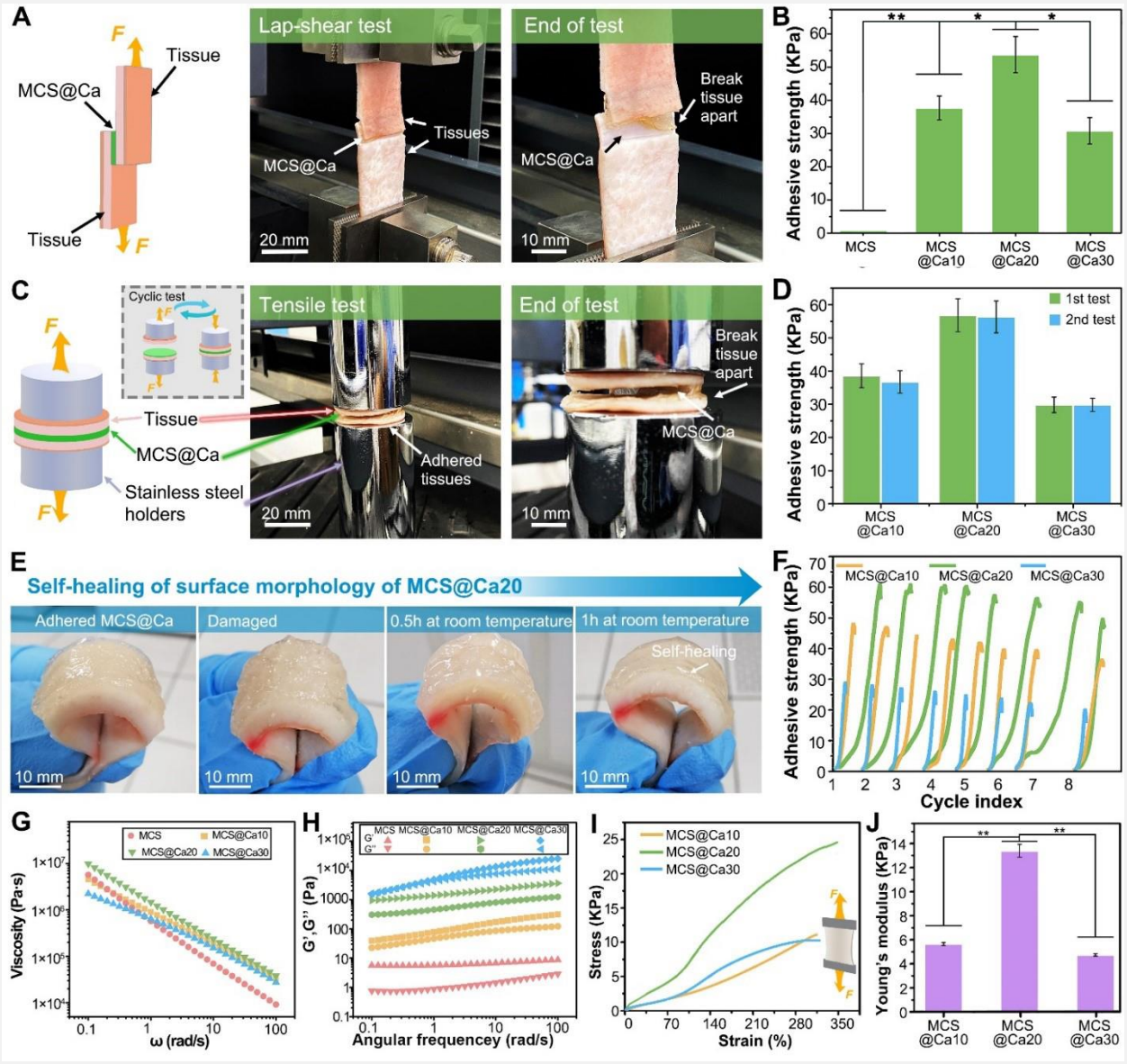

Figure 4. A) Self-established model for lap shear test. B) Adhesive strength of lap shear (*$p < 0.05$). C) Self-established model for recuperative and repeated detach-adhere tests. D) Recuperative adhesive strength. E) Images of MCS@Ca adhered to porcine skin during recuperative cyclic adhesion tests. F) Adhesive strength via repeated cyclic adhesion test. Values represent the mean ± standard deviation (n = 3–5). G) Rheological analysis of viscosity changes. The data were shifted along the vertical axis by 10^a to avoid overlapping ($a_{MCS} = -2$, $a_{MCS@Ca10} = -1$ $a_{MCS@Ca20} = 0$, $a_{MCS@Ca30} = 1$. H) Rheological analysis of G' and G'' changes. I) Stress–strain behavior. J) Young's modulus. Values represent the mean and standard deviation (n=3-5) (**$p<0.01$).

To further test the adhesion performance of MCS@Ca, recuperative adhesion tests were performed (Figure 4C). Following the second round of testing, the adhesion of MCS@Ca10 recovered to more than 90%, whereas the adhesive strength of MCS@Ca20 and MCS@Ca30 fully recovered (Figure 4D). The macro morphology of MCS@Ca20 during the recuperative cyclic adhesion tests was also observed **(**Figure 4E). After the first loading test, the morphology of MCS@Ca was damaged, and its surface contained many small raised areas that resulted in a rough texture. However, after 1 h reconversion, the surface of MCS@Ca became smooth again, indicating that MCS@Ca had the ability to self-recover (Wang et al., 2019a). Utilizing this feature, MCS@Ca may potentially reduce the risk of accidental damage caused by surgical adhesive during wound healing, thereby enhancing the overall treatment efficiency. Apart from the self-recovery feature, this phenomenon also suggested good conformance to irregular surfaces upon adhesion. Spontaneous conformance of the attached material to irregular surfaces could avoid detachment between the two distinct materials by interlocking and/or increased friction between the two surfaces (Park et al., 2017a). MCS@Ca also exhibited adhesive stability over eight cycles in the repeated continuous adhere-detach test (Figure 4C). As shown in Figure 4F, MCS@Ca20 retained approximately 80.65% of its original adhesive strength after the eighth cycle, while MCS@Ca10 retained 75.00% and MCS@Ca30 retained 68.97%. Even for MCS@Ca30, with the lowest retention of original adhesion translating to an adhesive strength of 20.06 kPa, its adhesive performance is equivalent to that of various previously reported fiber adhesives (Yuk et al., 2019). Thus, MCS@Ca exhibited stable adhesive properties.

The superior fitting performance could also be a result of the viscosity and modulus of the MCS@Ca materials, which are shown in Figure 4G. The viscosity of MCS@Ca was higher than that of MCS,

indicating that Ca^{2+} chelation endowed MCS@Ca with a more stable hydrogel structure. Notably, high viscosity is indicative of high adhesion (Li et al., 2018). In addition, the elastic modulus (G') of MCS@Ca also increased following the Ca-FA treatment (Figure 4H), suggesting that the entangled network structure in the hydrogel substrate was enriched (Yin et al., 2017). Among all three MCS@Ca materials, the mechanical properties, in terms of the tensile strength, elongation (Figure 4I), and Young's modulus (Figure 4J), of MCS@Ca20 were superior. Considering both its outstanding adhesive and mechanical properties, MCS@Ca20 was selected for subsequent experiments.

In practical applications, adhesiveness to various substrates is an essential factor (Gan et al., 2019). As shown in Figure 5A, MCS@Ca20 demonstrated outstanding dry adhesive properties to metal, plastic, rubber, wood, and glass, which effectively prevented these objects from falling due to gravity. To assess the wet adhesion capacity of MCS@Ca20 to fresh organs, pig kidneys was used as the tissue model (Figure 5B). MCS@Ca20 exhibited high extensibility and flexibility, and it did not peel off upon bending, twisting, and washing. Hence, the mechanical properties supported the adhesion performance of MCS@Ca20. Moreover, the tensile test confirmed that the material was readily elongated without breakage (Figure 5C**)** with the elongation and tensile strength reaching approximately 350% and 25 kPa, respectively; its Young's modulus was as high as 13.4 kPa, confirming its anti-breakage properties (Figure 5D). In addition, the application of MCS@Ca20 to the base of a human palm revealed that it effectively adhered to the wrinkles and folds of skin (Figure 5E), and the surface transformation than in the case of the kidney. To examine the interface between MCS@Ca20 and the tissue after adhesion, microscopic images (optical and fluorescence) of MCS@Ca20-adhered porcine skin were immediately captured (Figure 5F(a)). For comparison, the images following 1 h of adhesion were also collected. The interface between porcine skin and

MCS@Ca20 became indistinct (Figure 5F(b)) as MCS@Ca20 slightly swelled because of material diffusion across the interface. This swelling of MCS@Ca20 and concomitant diffusion of materials across the interface corroborated the postulate made in relation to Figure 4E. The spontaneous fitting of MCS@Ca20 to the irregular surface occurred because of the interlocking interface, which provided a safeguard to reduce the chance of MCS@Ca20 peeling off during the subsequent adhesion process.

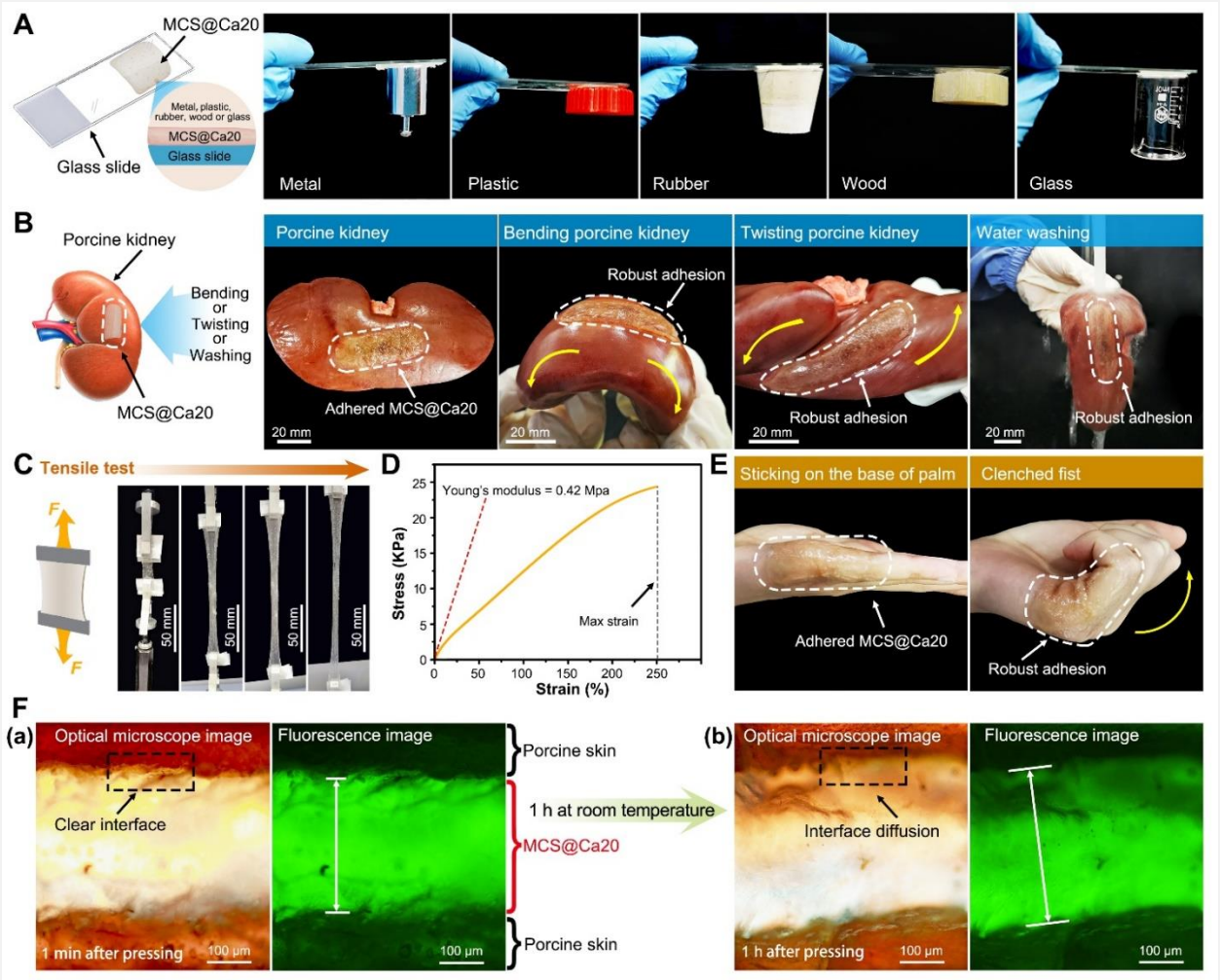

Figure 5. A) MCS@Ca20 adhered to different substrates. B) MCS@Ca20 adhered to pig kidney under different conditions. C) MCS@Ca20 during elongation test. D) Stress–strain profiles of MCS@Ca20. E) MCS@Ca20 adhered to the base of a human palm. F) Optical and fluorescence microscopy images of MCS@Ca20 adhered to porcine skin: (a) immediately after adhesion and (b)

1 h after adhesion.

3.3 In vivo experiments and histological analysis

In the *in vivo* experiment, a wound on the rabbit liver was first generated and then MCS@Ca20 was applied for healing (Figure 6A). The applied MCS@Ca20 was observed to adhere firmly onto the liver (Figure 6B). The appearance of MCS@Ca20 on days 14 and 28 after application is presented in Figure 6C. The MCS@Ca20 adhesive remained firmly attached under physiological conditions throughout the healing period. However, histological assessment on day 14 revealed tissue calcification, caused by Ca^{2+} ions, and fibroblast proliferation, representing wound healing progression (Park et al., 2017b). Meanwhile, MCS@Ca20 had undergone significant biodegradation after 28 days and was nearly fully dissolved after 42 days, indicating that the tissue had fully healed and that the intact connective tissue in the recovered rabbit liver resembled that of the healthy connective tissue (Figure 6D). Further, according to the live/dead cell staining test (Figure 6E) and MTT assay (Figure 6F), MCS@Ca20 was non-toxic and promoted cell growth. The cell viabilities were all more than 100% in the MTT assay.

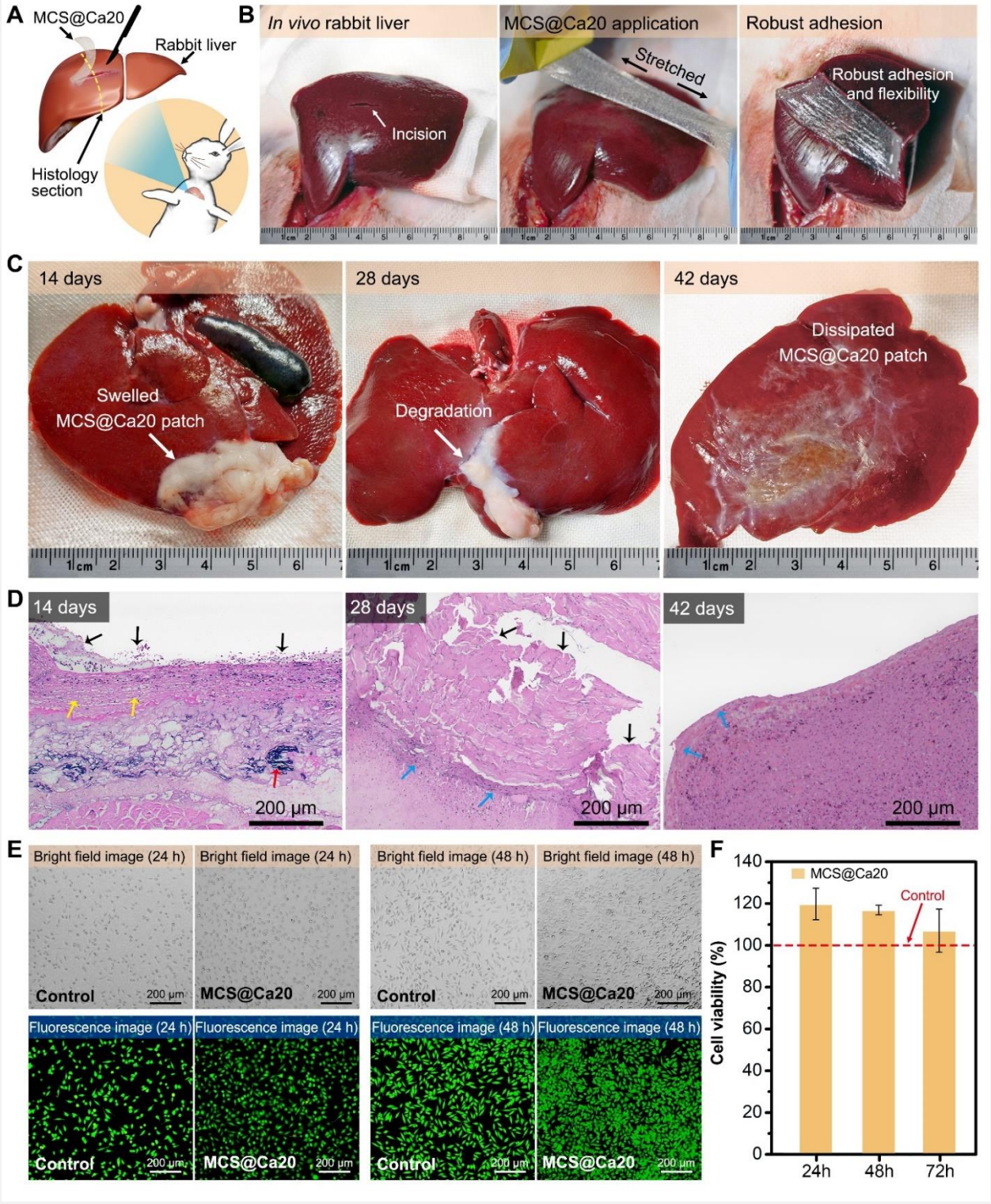

Figure 6. A) Liver wound model. B) Application of MCS@Ca20 over liver wound. C) Images of MCS@Ca20-adhered liver during healing. D) H&E tissue staining images of the MCS@Ca20-adhered liver (Red arrows: tissue calcification; yellow arrows: fibroblast; blue arrows: healed surface of the rabbit liver; black arrows: residual MCS@Ca). E) Bright field and fluorescent images of

live/dead cell staining. The green fluorescence represents live cells, while the red fluorescence represents dead cells. F) Biocompatibility of MCS@Ca in L929 cells via the MTT assay. Values represent the mean and standard deviation (n=3-5).

The *in vivo* biodegradability of MCS@Ca20 in a rabbit back muscle implantation model was further evaluated (Figure 7) using Sorbalgon® as a control. Macroscopic observation revealed that the control group showed more severe inflammation in the back muscles (Figure 7A). On day 14, the Sorbalgon® group developed an abscess, while the MCS@Ca20 group showed sustained wound healing. However, on day 28, although the abscess in the MCS@Ca20 group had enlarged, similar to that observed for the control (Sorbalgon®) group, it had become significantly reduced in size by day 42 and had disappeared by day 56; meanwhile, the abscess was still present in the Sorbalgon® group on day 56. The degradation of the underlying tissue (beneath MCS@Ca20 and Sorbalgon®) was further examined via histological assessments (Figure 7B). On day 14, pieces of residual samples as well as mild inflammatory responses were observed in both the Sorbalgon® and MCS@Ca20 groups; however, the Sorbalgon® group showed tissue calcification, which was absent in the MCS@Ca20 group. Additionally, the level of inflammation slowly reduced over time with substantial continuous degradation of MCS@Ca20 and Sorbalgon® until day 42, at which time the amount of residual MCS@Ca20 and Sorbalgon® had significantly decreased and tissue calcification was observed in the MCS@Ca20 group. The relatively fast-degrading MCS@Ca20 group showed no signs of sample residue in the rabbits on day 56, while the relatively slow-degrading control group presented with a blue non-tissue structure, believed to be the degradation product of Sorbalgon®. Overall, these results indicate that MCS@Ca20 possesses outstanding biocompatibility and biodegradability properties.

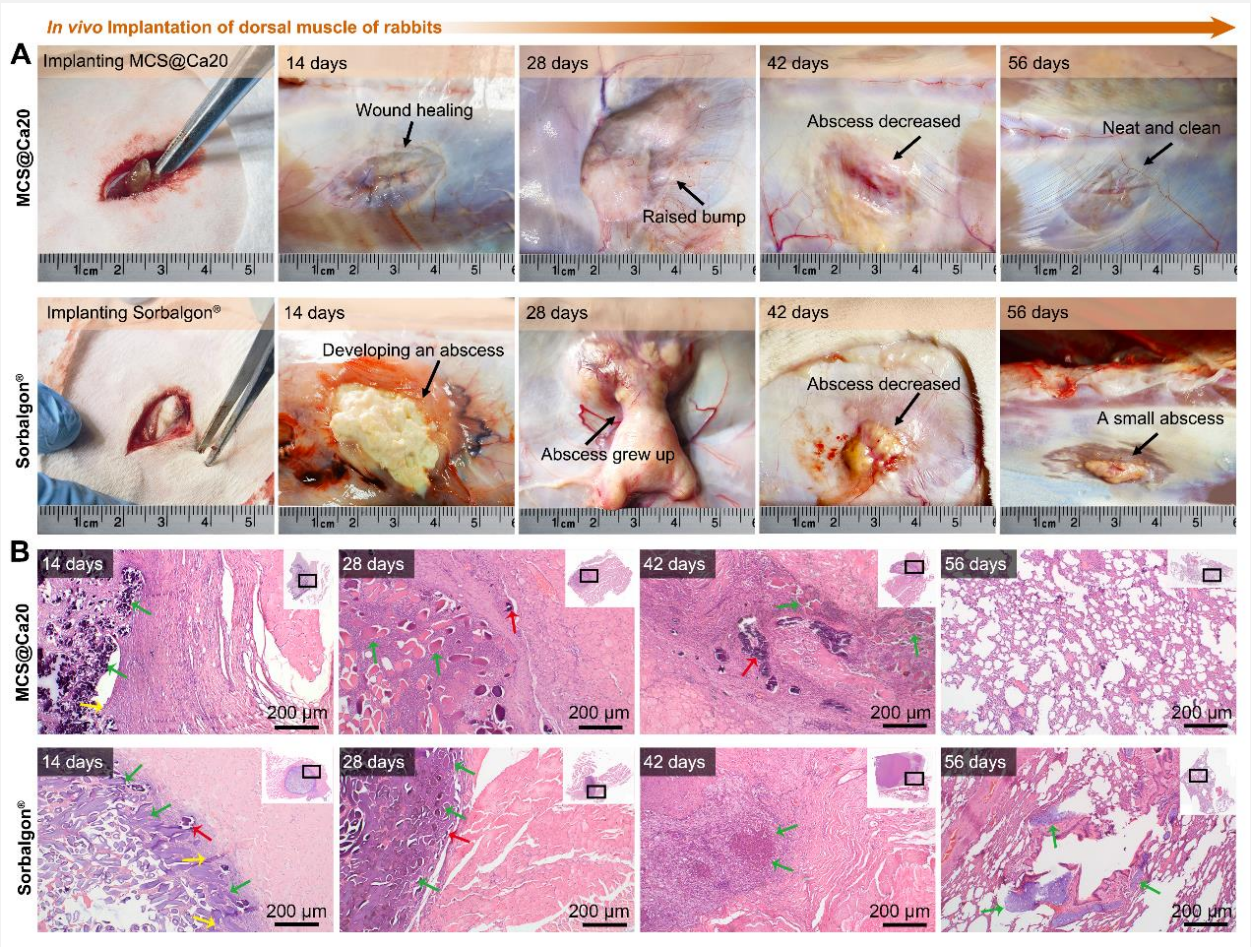

Figure 7. A) MCS@Ca20 and Sorbalgon® implanted into the dorsal subcutaneous muscle. B) H&E tissue staining of Sorbalgon® and MCS@Ca20 tissues (Green arrows: residual samples; yellow arrows: inflammatory response; red arrows: tissue calcification).

3.4 Sealant performance of MCS@Ca20

Although MCS@Ca20 demonstrated excellent adhesion performance in the liver wound model, the response of other tissues and organs may be quite distinct. For example, unlike liver or kidney, the stomach and heart contain liquids, which may leak in case of accidental damage. Thus, sealing performance is another critical consideration. In addition to satisfactory adhesion performance, successful sealing demands that the material must effectively sustain dynamic and static pressures

under wet physiological conditions without leakage. In this regard, an *ex vivo* porcine model was adopted to assess the anti-leaking (sealing) performance of MCS@Ca20.

MCS@Ca20 was first adhered to a fluid-filled punctured porcine stomach (Figure 8A**)**. Following adhesion of MCS@Ca20, the damaged porcine stomach stopped leaking, demonstrating the remarkable liquid-sealing properties of MCS@Ca20. Although a small blister formed in MCS@Ca20 due to pressure, it was not breached by the water pressure. Following the removal of water from the damaged stomach, MCS@Ca20 recovered its initial form and remained firmly adhered to the tissue. To demonstrate the feasibility of using MCS@Ca20 a sealant on dynamic surfaces *in vivo*, we used a porcine heart (Figure 8B). The MCS@Ca20 adhered heart was filled with red ink, and a stretchable pressure sensor was utilized to detect the output pressure applied at the punctured site during simulated heart beating. The results showed that MCS@Ca20 sustained steady pressure over 20 circulation cycles, suggesting that MCS@Ca20 can serve as an adhesive medium for smart wearable or implantable electronic devices applied to wet or dynamic tissues without sacrificing sensing signals (Yuk et al., 2019). In some cases, damaged organs may also release gas. For example, people will hiccup as a result of gas accumulation in the stomach while digesting various foods. Consequently, to assess the sealing performance of MCS@Ca20 against air-leakage, we applied it onto a punctured balloon (Figure 8C). Intuitively, it was not possible to inflate the balloon without the sealant; however, it was readily inflated following the application of MCS@Ca20, which adapted to accommodate the inflation, demonstrating its excellent air-sealing feature and flexibility (Video S1). Sealing of the blowing balloon due to robust adhesion can be explained by the Kendall theory, where the potential peeling angles for MCS@Ca20 was ultra-small (Gu et al., 2016). Therefore, MCS@Ca20 demonstrated outstanding fluid-sealing, air-sealing, and adhesion to dynamic tissues. Furthermore, in

contrast to other adhesive hydrogels, it did not require the application of additives (Liu et al., 2017) or preloading (Chen et al., 2019) to enhance its adhesive properties. Thus, it provides numerous merits over existing bio-sealants and adhesives for tissues, including its stretchability, robust adhesive performance, and rapid adhesion formation, which facilitated tissue and organ repair.

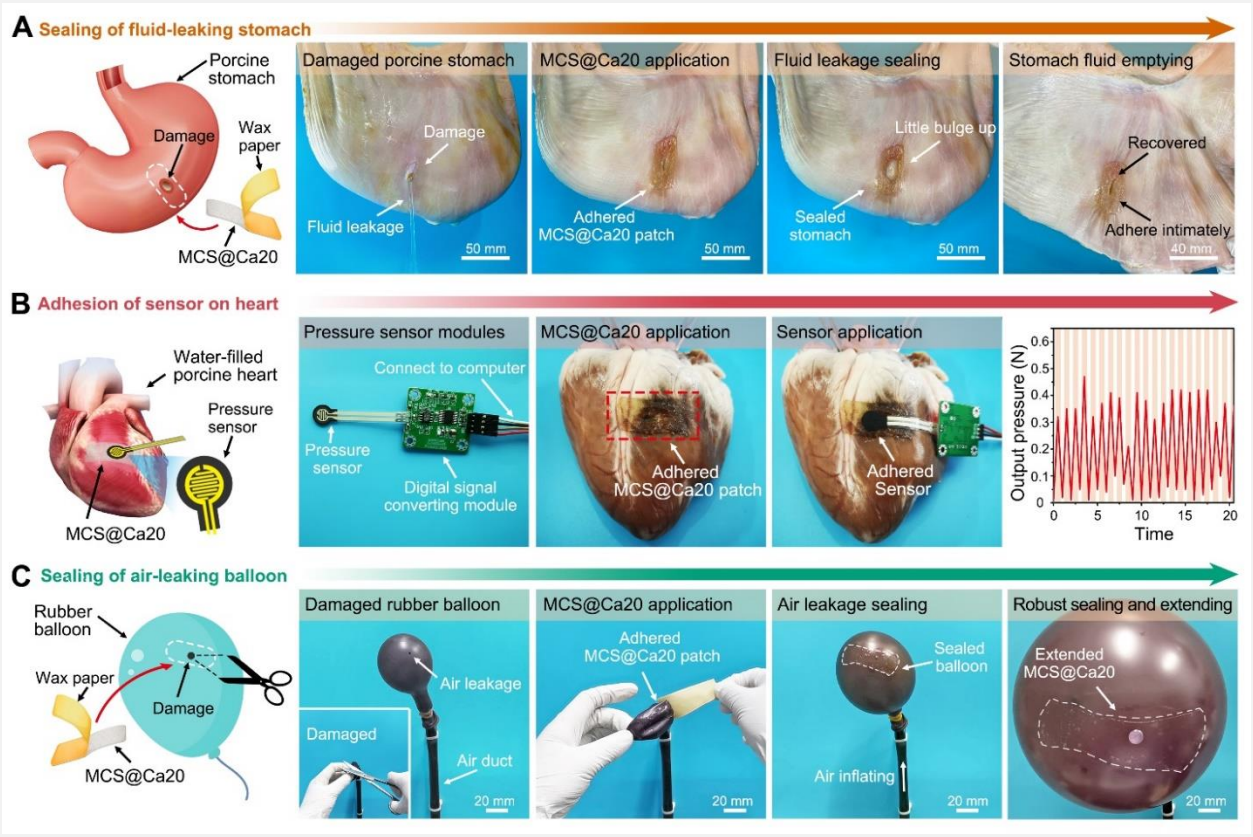

Figure 8. A) Sealing of broken porcine stomach. B) Sealing of broken porcine heart and adhesion of pressure sensor. C) Sealing of an air-leaking balloon.

3.5 Perspectives and Prospects

The biomaterials industry is thriving worldwide, and research in advanced biomaterials and life sciences has attracted considerable attention in the past years. As most regions of the world face ageing populations, an increase in the consumption of biomaterials for medical applications is anticipated. Moreover, a circular economy is important for sustainable growth (Habagil et al., 2020).

Therefore, transforming disqualified silk fibers to bioadhesives is a significant undertaking. According to the present study, silk wastes, which are produced in significant amounts by the huge textile industry in China, can be transformed into valuable resources for the manufacture of biomaterials. Unfortunately, similar investigations have not been conducted. Therefore, future research directions may focus on the impacts of the physical form of silk-waste-nonwoven fabrics on the adhesion performance of the resulting biomaterial. In particular, fabric density, fabric thickness, and fiber length may influence the adhesiveness, strength, and elasticity of bioadhesives, which are critical for tissue amendment. However, some barriers may exist in the supply chain of "wastes-to-resources". For example, conventional textile mills are currently incapable of manufacturing biomaterials from silk wastes, and there are no existing supply chains to deliver silk wastes from textile mills to biomaterial manufacturing factories. Furthermore, other gaps that impede the circulation of silk wastes between the textile and biomaterials industries include economics, social acceptance, and regulations. To overcome these obstacles, initiatives that establish policies, provide economic incentives, and develop performance evaluation system are required (Pan et al., 2015).

4. Conclusion

Bioadhesives are critical for tissue repair, particularly when tissues are severely damaged. This study developed an instant transparent adhesive with high stretchability, biocompatibility, and biodegradation, namely MCS@Ca, via a convenient approach for tissue repair. The adhesiveness of MCS@Ca was generated via Ca^{2+} acting as a crosslinker of silk to form metal-chelate complexes and water-capturing sites. Therefore, the adhesive properties of MCS@Ca can be controlled by adjusting the $CaCl_2$:FA mass ratio during the surface treatment of MCS. Since containing the optimum Ca^{2+}

content, the typical MCS@Ca20 sample (elongation of 350%, tensile strength of 25 kPa, and Young's modulus of 13.4 kPa) exhibited superior adhesion performance (as high as 54 kPa) for the highest random coil content and the lowest β-sheet content present in its silk substrates, making MCS@Ca20 much more competitive than previously reported adhesives. MTT assays were conducted to demonstrate biocompatibility of MCS@Ca, which showed that the cell viabilities were all more than 100%. Animal testing further demonstrated the superior repair performance (injured liver recovered in 42 days) and biodegradability (totally degraded in 56 days) of MCS@Ca compared with that of the commercially available product Sorbalgon®. In addition, the material can serve as an excellent bio-sealant to prevent liquid and/or gas leakage. The present study shifts the focus regarding the destiny of natural textile nonwovens from low-value blended textiles to value-added biomaterials by eliminating the complicated dissolution processes used to extract SFs. The facilely prepared silk biomaterials, with superior instant adhesiveness and sealing performance, offer an alternative to conventional suturing. More importantly, they demonstrate that natural silk nonwovens can be transformed into biomaterials, offering a route to upcycle disqualified waste silk fibers.

Acknowledgments

This work was supported by the National Natural Science Foundation of China [grant numbers 51803170, 51703185, and 51803171] and the Fundamental Research Funds for the Central Universities [grant numbers XDJK2018C030, XDJK2019AC003, and XDJK2020B017].

Conflict of Interest

The authors declare no conflicts of interest.

References

Annabi, N., Rana, D., Shirzaei Sani, E., Portillo-Lara, R., Gifford, J.L., Fares, M.M., Mithieux, S.M., Weiss, A.S., Engineering a sprayable and elastic hydrogel adhesive with antimicrobial properties for wound healing, Biomaterials (2017). 10.1016/j.biomaterials.2017.05.011.

Bai, S., Zhang, X., Cai, P., Huang, X., Huang, Y., Liu, R., Zhang, M., Song, J., Chen, X., Yang, H., A silk-based sealant with tough adhesion for instant hemostasis of bleeding tissues, Nanoscale Horizons (2019a). 10.1039/c9nh00317g.

Bai, S., Zhang, X., Lv, X., Zhang, M., Huang, X., Shi, Y., Lu, C., Song, J., Yang, H., Bioinspired Mineral–Organic Bone Adhesives for Stable Fracture Fixation and Accelerated Bone Regeneration, Advanced Functional Materials (2019b). 10.1002/adfm.201908381.

Brennan, M.J., Kilbride, B.F., Wilker, J.J., Liu, J.C., A bioinspired elastin-based protein for a cytocompatible underwater adhesive, Biomaterials (2017). 10.1016/j.biomaterials.2017.01.034.

Burke, K.A., Roberts, D.C., Kaplan, D.L., Silk Fibroin Aqueous-Based Adhesives Inspired by Mussel Adhesive Proteins, Biomacromolecules (2016). 10.1021/acs.biomac.5b01330.

Chen, W., Wang, R., Xu, T., Ma, X., Yao, Z., Chi, B., Xu, H., A mussel-inspired poly(γ-glutamic acid) tissue adhesive with high wet strength for wound closure %J Journal of Materials Chemistry B, Journal of Materials Chemistry B (2017). 10.1039/C7TB00813A.

Chen, X., Yuk, H., Wu, J., Nabzdyk, C.S., Zhao, X., Instant tough bioadhesive with triggerable benign detachment, Proceedings of the National Academy of Sciences (2020). 10.1073/pnas.2006389117.

Chen, Y., Meng, J., Gu, Z., Wan, X., Jiang, L., Wang, S., Bioinspired Multiscale Wet Adhesive Surfaces: Structures and Controlled Adhesion, Advanced Functional Materials (2019). 10.1002/adfm.201905287.

Cheng, L., Li, Z., Liu, Z., Chen, S., Bao, Y., Gao, L., Tong, X., Dai, F., Enhanced thermal and mechanical properties of natural silkworm cocoon composites constructed by multi-silkworm larvae simultaneously, Materials Letters (2019). 10.1016/j.matlet.2019.03.108.

Costa, R.R., Soares da Costa, D., Reis, R.L., Pashkuleva, I., Bioinspired baroplastic glycosaminoglycan sealants for soft tissues, Acta Biomater (2019). 10.1016/j.actbio.2019.01.040.

Cui, C., Wu, T., Chen, X., Liu, Y., Li, Y., Xu, Z., Fan, C., Liu, W., A Janus Hydrogel Wet Adhesive for Internal Tissue Repair and Anti-Postoperative Adhesion, Advanced Functional Materials (2020). 10.1002/adfm.202005689.

Deng, J., Tang, Y., Zhang, Q., Wang, C., Liao, M., Ji, P., Song, J., Luo, G., Chen, L., Ran, X., Wei, Z., Zheng, L., Dang, R., Liu, X., Zhang, H., Zhang, Y.S., Zhang, X., Tan, H., A Bioinspired Medical Adhesive Derived from Skin Secretion of Andrias davidianus for Wound Healing, Advanced Functional Materials (2019). 10.1002/adfm.201809110.

Drnovšek, N., Kocen, R., Gantar, A., Drobnič-Košorok, M., Leonardi, A., Križaj, I., Rečnik, A., Novak, S., Size of silk fibroin β-sheet domains affected by Ca2+, Journal of Materials Chemistry B (2016). 10.1039/c6tb01101b.

Gan, D., Huang, Z., Wang, X., Jiang, L., Wang, C., Zhu, M., Ren, F., Fang, L., Wang, K., Xie, C., Lu, X., Graphene Oxide-Templated Conductive and Redox-Active Nanosheets Incorporated Hydrogels for Adhesive Bioelectronics, Advanced Functional Materials (2019). 10.1002/adfm.201907678.

Gao, L., Zhou, Y., Peng, J., Xu, C., Xu, Q., Xing, M., Chang, J., A novel dual-adhesive and bioactive hydrogel activated by bioglass for wound healing, NPG Asia Materials (2019). 10.1038/s41427-019-0168-0.

Ghobril, C., Grinstaff, M.W., The chemistry and engineering of polymeric hydrogel adhesives for wound closure: a tutorial, Chem Soc Rev (2015). 10.1039/c4cs00332b.

Gu, Z., Li, S., Zhang, F., Wang, S., Understanding Surface Adhesion in Nature: A Peeling Model, Advanced Science (2016). https://doi.org/10.1002/advs.201500327.

Guo, J., Kim, G.B., Shan, D., Kim, J.P., Hu, J., Wang, W., Hamad, F.G., Qian, G., Rizk, E.B., Yang, J., Click chemistry improved wet adhesion strength of mussel-inspired citrate-based antimicrobial bioadhesives, Biomaterials (2017). 10.1016/j.biomaterials.2016.10.010.

Habagil, M., Keucken, A., Sárvári Horváth, I., Biogas Production from Food Residues—The Role of Trace Metals and Co-Digestion with Primary Sludge, Environments (2020). 10.3390/environments7060042.

Han, L., Lu, X., Liu, K., Wang, K., Fang, L., Weng, L.T., Zhang, H., Tang, Y., Ren, F., Zhao, C., Sun, G., Liang, R., Li, Z., Mussel-Inspired Adhesive and Tough Hydrogel Based on Nanoclay Confined Dopamine Polymerization, ACS Nano (2017). 10.1021/acsnano.6b05318.

Han, L., Wang, M., Prieto-López, L.O., Deng, X., Cui, J., Self-Hydrophobization in a Dynamic Hydrogel for Creating Nonspecific Repeatable Underwater Adhesion, Advanced Functional Materials (2020). https://doi.org/10.1002/adfm.201907064.

He, X.Y., Sun, A., Li, T., Qian, Y.J., Qian, H., Ling, Y.F., Zhang, L.H., Liu, Q.Y., Peng, T., Qian, Z., Mussel-inspired antimicrobial gelatin/chitosan tissue adhesive rapidly activated in situ by H2O2/ascorbic acid for infected wound closure, Carbohydrate Polymers (2020). 10.1016/j.carbpol.2020.116692.

Hong, Y., Zhou, F., Hua, Y., Zhang, X., Ni, C., Pan, D., Zhang, Y., Jiang, D., Yang, L., Lin, Q., Zou, Y., Yu, D., Arnot, D.E., Zou, X., Zhu, L., Zhang, S., Ouyang, H., A strongly adhesive hemostatic hydrogel for the repair of arterial and heart bleeds, Nat Commun (2019). 10.1038/s41467-019-10004-7.

Huadong, G., Steps to the digital Silk Road, Nature (2018). 10.1038/d41586-018-01303-y.

Huang, J., Wang, L., Jin, Y., Lu, P., Wang, L.L., Bai, N., Li, G., Zhu, P., Wang, Y., Zhang, J., Wu, Z., Guo, C.F., Tuning the Rigidity of Silk Fibroin for the Transfer of Highly Stretchable Electronics, Advanced Functional Materials (2020). 10.1002/adfm.202001518.

Jin, H.J., Park, J., Karageorgiou, V., Kim, U.J., Valluzzi, R., Cebe, P., Kaplan, D.L., Water-Stable Silk Films with Reduced β-Sheet Content, Advanced Functional Materials (2005). https://doi.org/10.1002/adfm.200400405.

Johnston, E.R., Miyagi, Y., Chuah, J.-A., Numata, K., Serban, M.A., Interplay between Silk Fibroin's Structure and Its Adhesive Properties, ACS Biomaterials Science & Engineering (2018). 10.1021/acsbiomaterials.8b00544.

Kim, S., Peterson, A.M., Holten-Andersen, N., Enhanced Water Retention Maintains Energy Dissipation in Dehydrated Metal-Coordinate Polymer Networks: Another Role for Fe-Catechol Cross-Links?, Chemistry of Materials (2018). 10.1021/acs.chemmater.7b05246.

Kim, S.H., Lee, Y.J., Chao, J.R., Kim, D.Y., Sultan, M.T., Lee, H.J., Lee, J.M., Lee, J.S., Lee, O.J., Hong, H., Lee, H., Ajiteru, O., Suh, Y.J., Choi, H.S., Cho, Y.-J., Park, C.H., Rapidly photocurable silk fibroin sealant for clinical applications, NPG Asia Materials (2020). 10.1038/s41427-020-0227-6.

Li, A., Jia, Y., Sun, S., Xu, Y., Minsky, B.B., Stuart, M.A.C., Co¨lfen, H., von Klitzing, R., Guo, X., Mineral-Enhanced Polyacrylic Acid Hydrogel as an Oyster-Inspired Organic–Inorganic Hybrid Adhesive, ACS Applied Materials & Interfaces (2018). 10.1021/acsami.8b01082.

Li, J., Celiz, A.D., Yang, J., Yang, Q., Wamala, I., Whyte, W., Seo, B.R., Vasilyev, N.V., Vlassak, J.J., Suo, Z.J.E., Tough adhesives for diverse wet surfaces, Science (2017).

Lin, J., Cai, X., Tang, M., Wang, S., Preparation and Evaluation of the Chelating Nanocomposite Fabricated with Marine Algae Schizochytrium sp. Protein Hydrolysate and Calcium, Journal of Agricultural and Food Chemistry (2015). 10.1021/acs.jafc.5b04001.

Ling, S., Zhang, Q., Kaplan, D.L., Omenetto, F., Buehler, M.J., Qin, Z., Printing of stretchable silk membranes for strain measurements, Lab on a Chip (2016). 10.1039/C6LC00519E.

Liu, C., Liu, X., Liu, C., Wang, N., Chen, H., Yao, W., Sun, G., Song, Q., Qiao, W., A highly efficient, in situ wet-adhesive dextran derivative sponge for rapid hemostasis, Biomaterials (2019). 10.1016/j.biomaterials.2019.03.016.

Liu, X., Yang, Y., Niu, X., Lin, Q., Zhao, B., Wang, Y., Zhu, L., An in situ photocrosslinkable platelet rich plasma - Complexed hydrogel glue with growth factor controlled release ability to promote cartilage defect repair, Acta Biomater (2017). 10.1016/j.actbio.2017.05.023.

Ming, Z., Fan, J., Bao, C., Xue, Y., Lin, Q., Zhu, L., Photogenerated Aldehydes for Protein Patterns on Hydrogels and Guidance of Cell Behavior, Advanced Functional Materials (2018). 10.1002/adfm.201706918.

Pan, S.-Y., Du, M.A., Huang, I.T., Liu, I.H., Chang, E.E., Chiang, P.-C., Strategies on implementation of waste-to-energy (WTE) supply chain for circular economy system: a review, Journal of Cleaner Production (2015). https://doi.org/10.1016/j.jclepro.2015.06.124.

Park, H.-H., Seong, M., Sun, K., Ko, H., Kim, S.M., Jeong, H.E., Flexible and Shape-Reconfigurable Hydrogel Interlocking Adhesives for High Adhesion in Wet Environments Based on Anisotropic Swelling of Hydrogel Microstructures, ACS Macro Letters (2017a). 10.1021/acsmacrolett.7b00829.

Park, S.R., Kim, J.W., Jun, H.S., Roh, J.Y., Lee, H.Y., Hong, I.S.J.M.T., Stem Cell Secretome and Its Effect on Cellular Mechanisms Relevant to Wound Healing, Molecular Therapy (2017b).

Qiu, W., Patil, A., Hu, F., Liu, X.Y., Hierarchical Structure of Silk Materials Versus Mechanical Performance and Mesoscopic Engineering Principles, Small (2019). 10.1002/smll.201903948.

Ryu, J.H., Kim, H.J., Kim, K., Yoon, G., Wang, Y., Choi, G.S., Lee, H., Park, J.S., Multipurpose Intraperitoneal Adhesive Patches, Advanced functional materials (2019). 10.1002/adfm.201900495.

Seo, J.-W., Kim, H., Kim, K., Choi, S.Q., Lee, H.J., Calcium-Modified Silk as a Biocompatible and Strong Adhesive for Epidermal Electronics, Advanced Functional Materials (2018). 10.1002/adfm.201800802.

Sun, H., Marelli, B., Polypeptide templating for designer hierarchical materials, Nat Commun (2020). 10.1038/s41467-019-14257-0.

Taddei, P., Tozzi, S., Zuccheri, G., Martinotti, S., Ranzato, E., Chiono, V., Carmagnola, I., Tsukada, M., Intermolecular interactions between B. mori silk fibroin and poly(l-lactic acid) in electrospun composite nanofibrous scaffolds, Materials Science and Engineering: C (2017). https://doi.org/10.1016/j.msec.2016.09.055.

Wang, Q., Ling, S., Liang, X., Wang, H., Lu, H., Zhang, Y., Self-Healable Multifunctional Electronic Tattoos Based on Silk and Graphene, Advanced Functional Materials (2019a). 10.1002/adfm.201808695.

Wang, Y., Wang, F., Xu, S., Wang, R., Chen, W., Hou, K., Tian, C., Wang, F., Yu, L., Lu, Z., Zhao, P., Xia, Q., Genetically engineered bi-functional silk material with improved cell proliferation and anti-inflammatory activity for medical application, Acta Biomater (2019b). 10.1016/j.actbio.2018.12.036.

Wei, W., Petrone, L., Tan, Y., Cai, H., Israelachvili, J.N., Miserez, A., Waite, J.H., An Underwater Surface-Drying Peptide Inspired by a Mussel Adhesive Protein, Adv Funct Mater (2016). 10.1002/adfm.201600210.

Wei, Y., Gong, R.H., Su, Z., Wang, X., Ding, X., Optimization and performance evaluation of silk fabrics dried in the domestic dryer, The Journal of The Textile Institute (2018). 10.1080/00405000.2017.1365579.

Xu, Y., Liang, K., Ullah, W., Ji, Y., Ma, J., Chitin nanocrystal enhanced wet adhesion performance of mussel-inspired citrate-based soft-tissue adhesive, Carbohydr Polym (2018). 10.1016/j.carbpol.2018.03.005.

Yin, Z., Wu, F., Zheng, Z., Kaplan, D.L., Kundu, S.C., Lu, S., Self-Assembling Silk-Based Nanofibers with Hierarchical Structures, ACS Biomaterials Science & Engineering (2017). 10.1021/acsbiomaterials.7b00442.

Yuk, H., Varela, C.E., Nabzdyk, C.S., Mao, X., Padera, R.F., Roche, E.T., Zhao, X., Dry double-sided tape for adhesion of wet tissues and devices, Nature (2019). 10.1038/s41586-019-1710-5.

Zhang, F., Lu, Q., Yue, X., Zuo, B., Qin, M., Li, F., Kaplan, D.L., Zhang, X., Regeneration of high-quality silk fibroin fiber by wet spinning from CaCl2-formic acid solvent, Acta Biomater (2015a). 10.1016/j.actbio.2014.09.045.

Zhang, M., Diethyl carbonate synthesis from CO2 with dehydrating agent of ethylene over catalysts of supported and mixed Ni–Cu@Na3PW12O40, Chemical Papers (2020). 10.1007/s11696-020-01262-7.

Zhang, M., A Novel Energy Band Match Method and a Highly Efficient CuO-Co3O4@SiO2 Catalyst for Dimethyl Carbonate Synthesis from CO2, Science of Advanced Materials (2021). 10.1166/sam.2021.3848.

Zhang, M., Xiao, M., Wang, S., Han, D., Lu, Y., Meng, Y., Cerium oxide-based catalysts made by template-precipitation for the dimethyl carbonate synthesis from Carbon dioxide and methanol, Journal of Cleaner Production (2015b). https://doi.org/10.1016/j.jclepro.2014.09.024.

Zhang, M., Xu, Y., Williams, B.L., Xiao, M., Wang, S., Han, D., Sun, L., Meng, Y., Catalytic materials for direct synthesis of dimethyl carbonate (DMC) from CO2, Journal of Cleaner Production (2021).

https://doi.org/10.1016/j.jclepro.2020.123344.
Zhou, L., Yu, K., Lu, F., Lan, G., Dai, F., Shang, S., Hu, E., Minimizing antibiotic dosage through in situ formation of gold nanoparticles across antibacterial wound dressings: A facile approach using silk fabric as the base substrate, Journal of Cleaner Production (2020). https://doi.org/10.1016/j.jclepro.2019.118604.